

# Observation of Temporal Reflections and Broadband Frequency Translations at Photonic Time-Interfaces

Hady Moussa<sup>1,2\*</sup>, Gengyu Xu<sup>1\*</sup>, Shixiong Yin<sup>1,2\*</sup>, Emanuele Galiffi<sup>1</sup>, Younes Ra'di<sup>1,3</sup> and Andrea Alù<sup>1,2,4</sup>

<sup>1</sup> Photonics Initiative, Advanced Science Research Center, City University of New York; New York, NY 10031, United States

<sup>2</sup> Department of Electric Engineering, City College of City University of New York; New York, NY 10031, United States

<sup>3</sup> Department of Electrical Engineering and Computer Science, Syracuse University, Syracuse, NY 13244, United States

<sup>4</sup> Physics Program, Graduate Center, City University of New York; New York, NY 10016, United States

Corresponding author. Email: [aalu@gc.cuny.edu](mailto:aalu@gc.cuny.edu)

\* These authors contributed equally to the work.

**Time-reflection is a uniform inversion of the temporal evolution of a signal, which arises when an abrupt change in the properties of the host material occurs uniformly in space.<sup>1-3</sup> At such a time-interface, a portion of the input signal is time-reversed, and its frequency spectrum is homogeneously translated while its momentum is conserved, forming the temporal counterpart of a spatial interface. Combinations of time-interfaces, forming time-metamaterials and Floquet matter<sup>4</sup>, exploit the interference among multiple time-reflections for extreme wave manipulation, leveraging time as a new degree of freedom<sup>5</sup>. Here, we report the observation of photonic time-reflections and associated broadband frequency translations in a switched transmission-line metamaterial whose effective capacitance is homogeneously and abruptly changed via a synchronized array of switches. A pair of temporal interfaces are combined to demonstrate time-reflection-induced wave interference, realizing the temporal counterpart of a Fabry-Perot cavity<sup>6</sup>. Our results establish foundational building blocks to realize time-metamaterials and Floquet photonic crystals, with opportunities for extreme photon manipulation in space and time<sup>7,8</sup>.**

Reflection is a universal phenomenon occurring when a traveling wave encounters an inhomogeneity. Spatial reflections arise at a sharp discontinuity in space: here, momentum is exchanged between an incoming wave and the interface, which acts as a momentum bath, while frequency is conserved. As the basis of wave scattering, spatial reflections play a key role in wave

control and routing, as well as in the formation of resonant modes, filtering, band engineering and metamaterial responses. Recently, advances across nonlinear wave sciences have stirred significant interest in the use of time as a new degree of freedom for wave scattering, leveraging time-varying media as reservoirs that mix and exchange energy with the waves in the system. As examples of these opportunities, photonic time-crystals and Floquet wave phenomena have raised interest across the broader physics community<sup>9–16</sup>. In this context, time-reflection (TR) constitutes the temporal counterpart of spatial reflection, with dual features. They occur at time-interfaces, i.e., when the properties of the host medium are switched homogeneously in space over a timespan much faster than the wave dynamics. Upon TR, an input wave is partly time-reversed: its energy and frequency content are generally transformed, while momentum is conserved because of spatial translational symmetry.

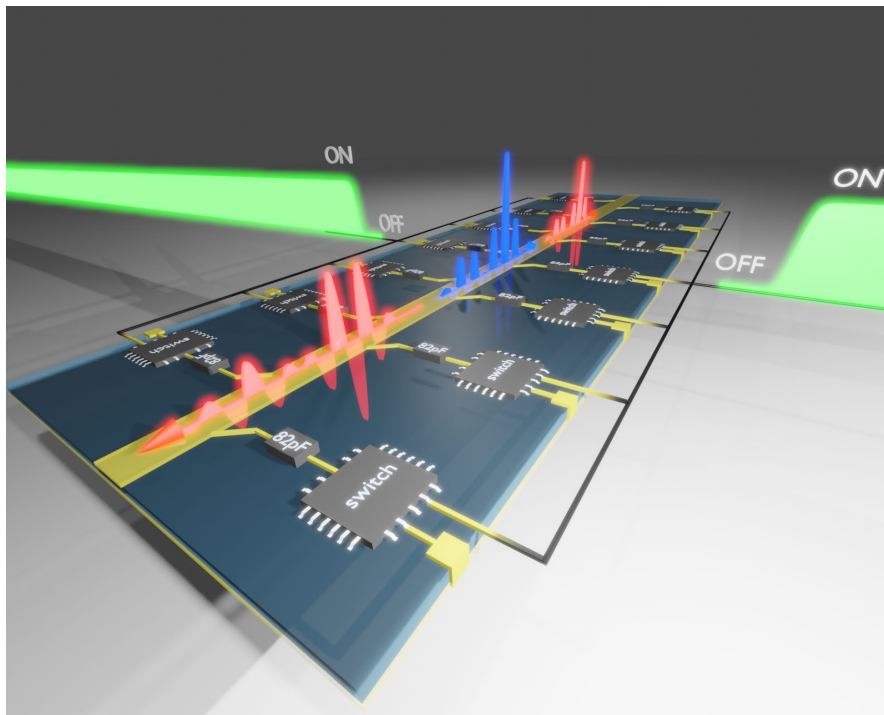


**Fig. 1:** Illustration of a time interface in a uniformly switched TLM. A step-like bias signal (in green) is used to uniformly activate a set of switches distributed along the TLM, with spacing much smaller than the wavelengths of operation. Upon closing the switches, the effective TLM impedance is abruptly decreased, causing a broadband forward-propagating signal (in blue) to be split into a time-transmitted and a time-reflected signal with redshifted frequencies (forward and backward red signals).

Time-reversal of an input wave has been demonstrated by periodically modulating the properties of the host medium at twice the frequency of the signal. This phenomenon has been observed in acoustics<sup>17</sup> and for electromagnetic waves, both at radio-frequencies<sup>18,19</sup> and in optics<sup>20</sup>. However, these parametric phenomena are inherently narrowband, relying on resonant coupling between positive and negative frequencies, and are subject to parametric instabilities, which lead to highly dispersive and nonlinear distortions. On the contrary, TRs at a time-interface enable broadband time-reversal and efficient frequency translation of an arbitrary waveform. While several exciting

theoretical proposals have been put forward to exploit these features for a variety of exotic photonic functionalities, including inverse prism<sup>21</sup>, temporal anti-reflection coatings and aiming<sup>6,22</sup>, so far time-interfaces have only been observed for water waves<sup>3</sup>, remaining elusive to photonics and thus drastically limiting their impact. The main challenge in this quest consists in the difficulty of imparting sufficiently strong variations of the material properties uniformly in space and with a temporal response much faster than the wave dynamics.

Here, we demonstrate time-interfaces and TRs in a microwave transmission-line metamaterial (TLM) periodically loaded by an array of lumped capacitors with a spacing significantly smaller than all wavelengths of interest. The loads are individually activated through voltage-controlled integrated switches, with temporal dynamics much faster than the relevant signal variations in time. At a switching event, the effective permittivity of the TLM is homogeneously and abruptly changed in time, while a broadband signal propagates through it, realizing a time-interface, with associated photonic TR and broadband efficient frequency translation, conceptually shown in Fig. 1. Next, we employ a pair of such time-interfaces to form a temporal slab, in which the reflected and transmitted signals at each time-interface interfere to demonstrate the temporal analogue of a Fabry-Perot filter<sup>6</sup>. Our results establish the fundamental building blocks to exploit time as a new degree of freedom for extreme wave manipulation in metamaterials<sup>4,5,23</sup>.

A photograph of our fabricated TLM is shown in Fig. 2A. A broadband input signal is injected from one of the ports, and travels along the meandered microstrip line, loaded by an array of switches connected in series to an array of subwavelength-spaced (unit cell length  $\approx 20.1$  cm) capacitors. The meandered microstrip emulates an unbounded medium with close-to-linear dispersion. While the signal is fully within the TLM, a control signal for the switches is sent via a pair of shorter microstrips, synchronously triggering all the switches with a rise-time  $\approx 5$  ns, much faster than the temporal dynamics of the incoming wave, which has a spectral width  $\approx 50$  MHz. This switching event results in a time interface.

At a spatial interface (Fig. 2B), translational symmetry is broken, hence the reflected waves undergo parity inversion ( $z \rightarrow -z$ ) and a receiver at the source location registers the features of a reflected signal in the same order as they were originally sent, akin to a sound echo. Frequency is conserved in this scenario, while wavevector and momentum are not. Conversely, at our time-interface (Fig. 2C) time-translation symmetry is broken while spatial symmetry is preserved. Hence, the “echo” associated with the time-reversed ( $t \rightarrow -t$ ) signal is detected backwards, while the signal retains its original spatial profile due to momentum conservation. In addition, the broadband frequency content of the input signal is abruptly transformed, as predicted by the band diagrams of our TLM shown in Fig. 2D. Blue and red lines depict the frequency dispersion before and after the switching, comparing simulated and measured results. Given the small spacing between neighboring loads compared to the relevant wavelengths, the curves follow a linear dispersion, with different slopes corresponding to the different effective capacitance before and after the switching. Wave scattering at a spatial discontinuity (Fig. 2B) is represented by a horizontal transition in the dispersion diagram (purple arrows in Fig. 2D, encompassing the broad

spectrum of the input signal), preserving frequency and generating waves with opposite momenta. Conversely, a time interface (Fig. 2C) corresponds to a vertical transition (green arrows in Fig. 2D), which preserves momentum and generates new positive and negative frequencies, efficiently converting the entire broadband spectrum of the input wave.

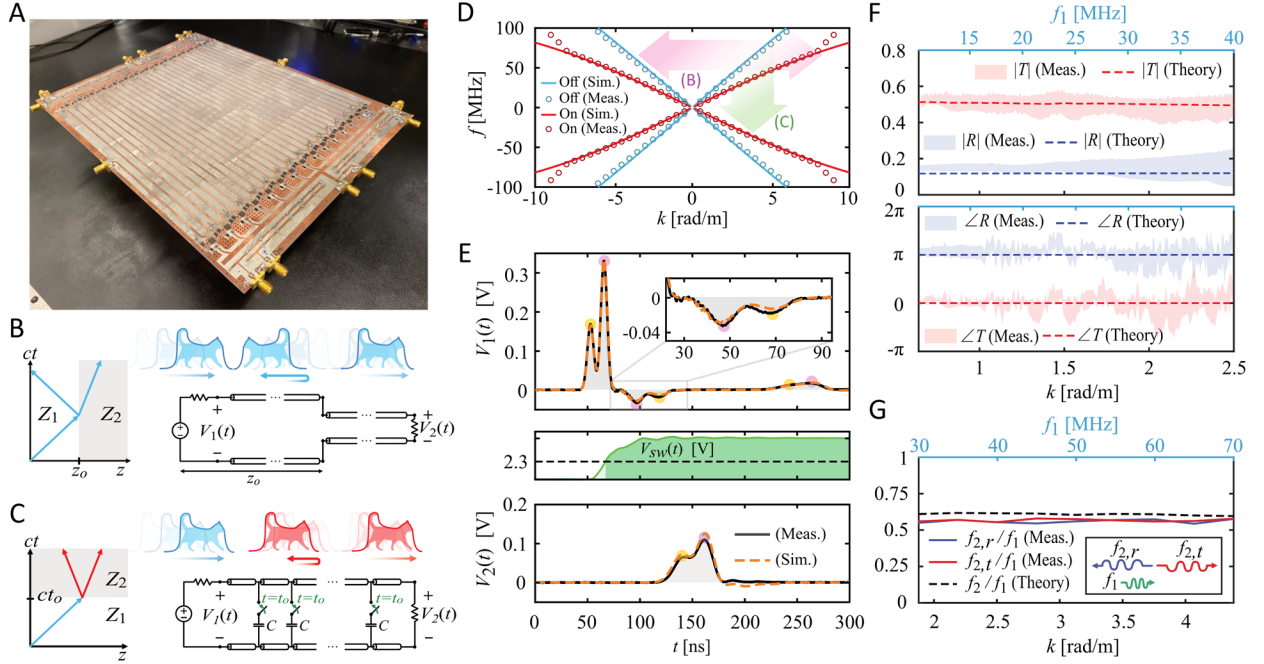


**Fig. 2. Experimental demonstration of a photonic time-reflection.** (A) Photo of the fabricated time-switched TLM. (B) Reflection at a spatial interface causes the reflected signal to invert its profile in space, while (C) a temporal interface breaks time-translation symmetry in a spatially homogeneous medium, uniformly inverting in time the propagation of an input signal. (D) Dispersion relation of the fabricated TLM (blue) before and (red) after activating the switches. Arrows indicate broadband transitions induced by (purple) spatial reflection, coupling positive and negative momenta, and (green) TR, coupling positive and negative frequencies. (E) Experimental observation of photonic TR at a time-interface. The input port voltage  $V_1$  shows a smaller input signal (yellow marker) followed by a larger one (purple marker). As the control signal  $V_{sw}$  (middle panel) reaches a threshold value (dashed horizontal line), a portion of the input signal undergoes TR, propagating back to the input port where the two signals are measured in reverse order, (purple marker, then yellow, see also zoomed inset). After  $\approx 140$  ns, the time-transmitted signal, after undergoing a spatial reflection at the end of the TLM, returns to the  $V_1$  port with identical order as the input signal (yellow marker, then purple). In the lower panel, the output-port voltage  $V_2$  shows the time-transmitted signal, undergoing temporal broadening due to a broadband redshift of its frequency content induced by the time-interface. (F) Amplitude (top) and phase (bottom) of the scattering spectra of the measured (shaded) and theoretical (dotted) time-transmission (T) and time-reflection (R) coefficients, measured by analyzing the Fourier spectrum of the time-scattered signals. (G) Measured and theoretical frequency translation occurring at the time-interface across the spectral content of the input signal.

These features are clearly observed in our experimental results (Fig. 2E): we excite the TLM with an input signal consisting of an asymmetric pair of Gaussian pulses, measured by the input port voltage  $V_1(t)$  as a first smaller pulse (yellow marker) followed by a larger one (purple marker).

Approximately 15 ns after the bias voltage  $V_{sw}$  has reached the switch activation threshold of 2.3 V (shown in the middle panel of Fig. 2E, see Supplementary Information on details of the timing), we record the time-reflected signal at the input port, whose zoomed-in view reveals it to be the TR-copy (purple  $\rightarrow$  yellow) of the input. This TR-signal has inverted polarity with respect to the input signal, indicating that the TR coefficient is negative, as expected for a reduction in wave impedance,  $R = Z_2(Z_2 - Z_1) / 2Z_1^2$  (see Methods for full derivation), where in our system  $Z_1 \approx 50\Omega$  is the line impedance before switching and  $Z_2 \approx 25\Omega$  is the line impedance after switching. Approximately 140 ns later, an attenuated signal is received at the input port, corresponding to the time-transmitted signal that has been traveling to the end of the TLM and then spatially reflected backwards at the mismatched termination. As expected, this second signal has inverted symmetry compared to the TR signal (yellow  $\rightarrow$  purple). The TR signal, as well as the time-transmitted signal at the output port  $V_2$  (Fig. 2E, bottom panel), preserve the same spatial profile as the incident signal due to preserved spatial symmetry, but they travel in a line with increased effective permittivity, hence they must slow down. This phenomenon underpins the broadband and highly efficient frequency translation process occurring abruptly at the time-interface, based on which each frequency component of the input signal is transformed according to  $\omega_1 \rightarrow \omega_2 = (Z_2 / Z_1)\omega_1$  (see Methods for derivation).

In Fig. 2F, we retrieve the TR and time-transmission coefficients (denoted as R and T, respectively) at the time-interface as a function of the input wavevector  $k$  (lower horizontal axis), and corresponding input frequency  $f_1$  (upper horizontal axis). Attenuation and phase accumulation occurring as the signals propagate in the TLM are accounted for in these calculations, as detailed in Methods. The reflection and transmission magnitude (top panel) and phase (bottom) agree well with theoretical predictions across the broadband input spectrum. As expected, the time-transmitted signal is in phase with the input, while the TR signal flips sign for all input momenta. Overall, our results confirm that the time-interface is sufficiently abrupt to generate a significant TR consistent with an instantaneous switching event. The weak wavelength-dispersion of the scattering coefficients at higher frequencies can be attributed to the finite switching speed, and to frequency dispersion associated to nonidealities of the circuit components and to the finite spacing between neighboring switches. We quantify the broadband nature of frequency translation at our photonic time-interface in Fig. 2G, in which we plot the measured frequency translation ratios for different signals with input carrier wavenumbers  $k$ , or equivalently frequencies  $f_1$ , spanning the interval 30-70 MHz (all with a fixed bandwidth of  $\approx 30$  MHz). The carrier frequencies of the time-reflected ( $f_{2,r}$ ) and time-transmitted ( $f_{2,t}$ ) signals are redshifted uniformly by  $\approx 55\%$ , as expected by the temporal spreading of the pulse widths in Fig. 2E. This value is consistent with the vertical transitions in Fig. 2D indicated by the green arrow.

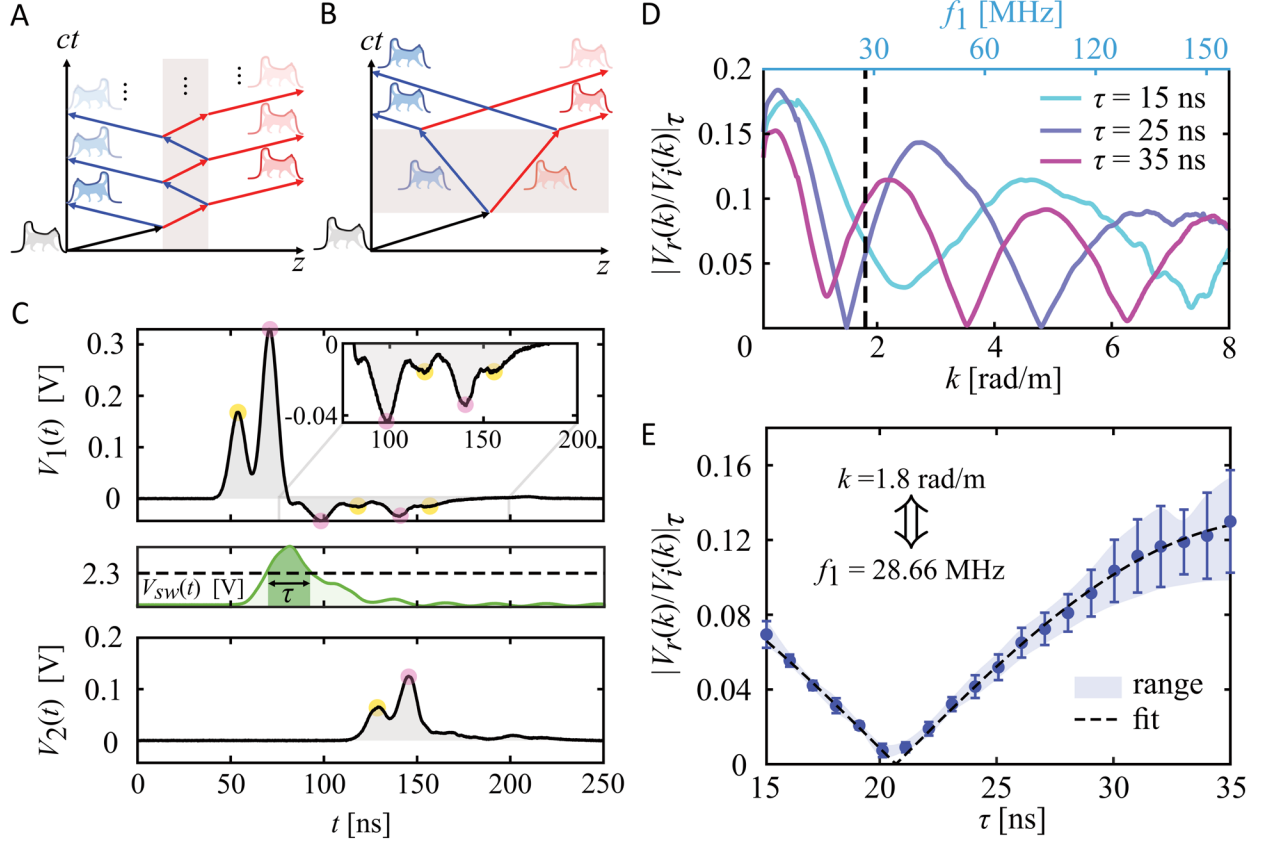


**Fig. 3. Wave scattering from a temporal slab.** (A) Conceptual sketches of a spatial and (B) a temporal slab with stepped wave impedance. Inside a spatial slab, multiple partial reflections occur, gradually decaying with increasing scattering orders, whereas at a temporal slab only four scattered waves interfere with each other. (C) Experimentally measured voltages at input ( $V_1$ ) and output ( $V_2$ ) ports after a temporal slab of duration  $\tau = 24$  ns. Two time-reversed signals with identical duration as the input signal are observed in  $V_1(t)$ , each having undergone TR. In the bottom plot, the first time-transmitted signal is followed by a much weaker signal, originated from the doubly TR signal. (D) Normalized amplitudes of the total TR signals as a function of wavenumber  $k$  for temporal slabs with  $\tau = 15$ , 25 and 35 ns, exhibiting zero reflection at selected frequencies, controlled by the slab duration  $\tau$ . (E) For fixed  $k$  (dotted vertical line in panel D), we measure the normalized reflection amplitude as a function of slab duration  $\tau$ , demonstrating large, continuous spectral tunability.

By combining multiple time-interfaces, it is possible to leverage TR-induced interference to manipulate more markedly the input signals. By combining two time-interfaces we form a temporal slab, realized by closing and reopening the switches after a delay  $\tau$ . These sequential TR events induce temporal wave interference. Due to causality, scattering phenomena at a temporal slab are markedly different from those in a spatial slab: while multiple scattering occurs in a spatial slab (Fig. 3A), generating a superposition of transmitted and reflected waves, a temporal slab produces a total of four scattered waves after the second time-interface (Fig. 3B). Our implementation of a temporal slab in a switched TLM shows some differences from temporal slabs theoretically considered in the recent literature<sup>14</sup>: in an ideal temporal slab in which the permittivity and/or permeability of an unbounded medium is abruptly switched, the electric

displacement  $\mathbf{D}$  and the magnetic induction  $\mathbf{B}$  are preserved<sup>1,2</sup>. In our TLM, these conditions would respectively correspond to the conservation of electric charge and magnetic flux. The initial closing of the switches, as in Fig. 2, indeed preserves the total charge in the TLM, since the lumped capacitors connected to the switches before the switching event are discharged. However, upon reopening the switches the now-charged capacitors are abruptly cut-off from the TLM at the second time-interface, producing a charge discontinuity while preserving voltage continuity. Hence, modified temporal boundary conditions need to be considered at this time-interface (see Methods).

In Fig. 3C an asymmetric signal interacts with a temporal slab of duration  $\tau = 24$  ns. Two TR signal pairs are measured in  $V_1(t)$ , each resulting from one TR and one time-transmission process, in opposite order. Notably, as opposed to conventional photonic time-interfaces<sup>24</sup>, both TR-signals here are out of phase with respect to the input signal, due to the different temporal boundary conditions when closing and reopening the switches, as discussed above and detailed in Methods. At the output port, the measured signal  $V_2(t)$  shows a large doubly transmitted signal, followed by a smaller feature due to a double TR process. Importantly, all the scattered signals have the same duration as the input signal, since the second time-interface converts back the frequency spectrum to the original frequencies, corresponding to two opposite vertical transitions in the band diagram.

The duration of the temporal slab can accurately control the output frequency content through wave interference between time-reflected and time-transmitted signals, realizing the temporal analogue of a Fabry-Perot etalon. To demonstrate this phenomenon, we study the total scattering amplitudes as a function of the temporal slab duration  $\tau$  and input wavenumber  $k$ . For different values of  $\tau$ , we Fourier-analyze the time-reflected waves, and plot their normalized momentum spectra  $|V_r(k)/V_i(k)|$  in Fig. 3D, where the subscripts  $i, r$  denote incident and reflected voltage amplitudes, respectively. For each slab duration, specific values of  $k$  feature zero reflection, due to destructive temporal interference between two TR waves, in analogy with the reflection zeros of a Fabry-Perot cavity. In this case, however, the associated phase accumulation does not occur in space, but rather in time. To further highlight the versatile wave control offered by our temporal slab through temporal interference, in Fig. 3E we examine the total TR at a fixed input wavenumber  $k = 1.8$  rad/m (dot-dashed vertical line in Fig. 3D), as we increase the slab duration, for six pulses of different half-maximum durations ranging from 5 ns to 10 ns, comparing measured and theoretical results. We observe how the total amplitude of the time-reversed waves can be continuously tuned by varying  $\tau$ , granting us dynamic control over wave interference at the two time-interfaces without having to change the lumped capacitance values.

To conclude, in this work we have reported the observation of photonic time-reflections and broadband efficient frequency translation at single and double time-interfaces, and the demonstration of controlled time-reversal-induced interference phenomena from a temporal slab formed by a pair of time-interfaces. This result establishes the key building block towards the

realization of time-metamaterials and photonic time crystals, opening a wide range of opportunities in the rising field of time-varying photonic media<sup>23</sup>, with applications for ultrafast wave routing and focusing<sup>3,22</sup>, negative refraction<sup>25,26</sup>, efficient and broadband frequency manipulation<sup>27</sup>, novel forms of ultrafast energy mixing<sup>28,29</sup>, and photonic Floquet matter<sup>4,12</sup>. Our TLM platform can be straightforwardly configured to introduce at the same time spatial and temporal interfaces, for instance by activating only a portion of the switches, thus blending together spatial and temporal degrees of freedom and enabling even more flexibility in wave control and manipulation.

## **Acknowledgments**

This work was supported by the Air Force Office of Scientific Research MURI program with grant No. FA9550-18-1-0379, the Simons Collaboration on Extreme Wave Phenomena and a Vannevar Bush Faculty Fellowship. E.G. was supported by the Simons Foundation through a Junior Fellowship of the Simons Society of Fellows (855344,EG).

## References

1. Morgenthaler, R. Velocity Modulation of Electromagnetic Waves. *IRE Trans. Microw. Theory Tech.* 167–172 (1958). doi:10.1109/TMTT.1958.1124533
2. Fante, R. L. Transmission of Electromagnetic Waves into Time-Varying Media. *IEEE Trans. Antennas Propag.* **AP-19**, 417–424 (1971).
3. Bacot, V., Labousse, M., Eddi, A., Fink, M. & Fort, E. Time reversal and holography with spacetime transformations. *Nat. Phys.* **12**, 972–977 (2016).
4. Yin, S., Galiffi, E. & Alù, A. Floquet metamaterials. *eLight* **2**, 8 (2022).
5. Engheta, N. Metamaterials with high degrees of freedom: Space, time, and more. *Nanophotonics* **10**, 639–642 (2021).
6. Pacheco-Peña, V. & Engheta, N. Antireflection temporal coatings. *Optica* **7**, 323–331 (2020).
7. Caloz, C. & Deck-Leger, Z.-L. Spacetime Metamaterials—Part I: General Concepts. *IEEE Trans. Antennas Propag.* **68**, 1569–1582 (2020).
8. Caloz, C. & Deck-Leger, Z.-L. Spacetime Metamaterials—Part II: Theory and Applications. *IEEE Trans. Antennas Propag.* **68**, 1583–1598 (2020).
9. Lustig, E., Segev, M. & Sharabi, Y. Topological aspects of photonic time crystals. *Opt. Vol 5 Issue 11 Pp 1390-1395* **5**, 1390–1395 (2018).
10. Lyubarov, M., Lumer, Y., Dikopoltsev, A., Lustig, E., Sharabi, Y. & Segev, M. Amplified emission and lasing in photonic time crystals. *Science* **0**, eabo3324 (2022).
11. Winn, J. N., Fan, S., Joannopoulos, J. D. & Ippen, E. P. Interband transitions in photonic crystals. *Phys. Rev. B* **59**, 1551–1554 (1999).
12. Dutt, A., Lin, Q., Yuan, L., Minkov, M., Xiao, M. & Fan, S. A single photonic cavity with two independent physical synthetic dimensions. *Science* **367**, 59–64 (2020).
13. Fleury, R., Khanikaev, A. B. & Alù, A. Floquet topological insulators for sound. *Nat. Commun.* **7**, 1–11 (2016).
14. Cartella, A., Nova, T. F., Fechner, M., Merlin, R. & Cavalleri, A. Parametric amplification of optical phonons. *Proc. Natl. Acad. Sci. U. S. A.* **115**, 12148–12151 (2018).
15. Shan, J.-Y., Ye, M., Chu, H., Lee, S., Park, J.-G., Balents, L. & Hsieh, D. Giant modulation of optical nonlinearity by Floquet engineering. *Nature* **600**, 235–239 (2021).
16. Hayran, Z., Chen, A. & Monticone, F. Spectral causality and the scattering of waves. *Optica* **8**, 1040 (2021).
17. Fink, M. & Prada, C. Acoustic time-reversal mirrors. *Inverse Probl.* **17**, R1–R38 (2001).
18. Chumak, A. V., Tiberkevich, V. S., Karenowska, A. D., Serga, A. A., Gregg, J. F., Slavin, A. N. & Hillebrands, B. All-linear time reversal by a dynamic artificial crystal. *Nat. Commun.* **1**, 141 (2010).
19. Lerosey, G., de Rosny, J., Tourin, A., Derode, A., Montaldo, G. & Fink, M. Time Reversal of Electromagnetic Waves. *Phys. Rev. Lett.* **92**, 193904 (2004).
20. Vezzoli, S., Bruno, V., Devault, C., Roger, T., Shalaev, V. M., Boltasseva, A., Ferrera, M., Clerici, M., Dubietis, A. & Faccio, D. Optical Time Reversal from Time-Dependent Epsilon-Near-Zero Media. *Phys. Rev. Lett.* **120**, 43902 (2018).
21. Akbarzadeh, A., Chamanara, N. & Caloz, C. Inverse prism based on temporal discontinuity and spatial dispersion. *Opt. Lett.* **43**, (2018).
22. Pacheco-Peña, V. & Engheta, N. Temporal aiming. *Light Sci. Appl.* **9**, 1–12 (2020).
23. Galiffi, E., Tirole, R., Yin, S., Li, H., Vezzoli, S., Huidobro, P. A., Silveirinha, M. G., Sapienza, R., Alù, A. & Pendry, J. B. Photonics of time-varying media. *Adv. Photonics* **4**, 014002 (2022).

24. Mendonça, J. T., Martins, A. M. & Guerreiro, A. Temporal beam splitter and temporal interference. *Phys. Rev. A* **68**, 043801 (2003).
25. Pendry, J. B. Time Reversal and Negative Refraction. *Science* **322**, 71–73 (2008).
26. Bruno, V., Devault, C., Vezzoli, S., Kudyshev, Z., Huq, T., Mignuzzi, S., Jacassi, A., Saha, S., Shah, Y. D., Maier, S. A., Cumming, D. R. S., Boltasseva, A., Ferrera, M., Clerici, M., Faccio, D., Sapienza, R. & Shalaev, V. M. Negative Refraction in Time-Varying Strongly Coupled Plasmonic-Antenna- Epsilon-Near-Zero Systems. *Phys. Rev. Lett.* **124**, 43902 (2020).
27. Miyamaru, F., Mizuo, C., Nakanishi, T., Nakata, Y., Hasebe, K., Nagase, S., Matsubara, Y., Goto, Y., Pérez-Urquizo, J., Madéo, J., Dani, K. M., Joel, P.-U., Mad'eo, J. & Dani, K. M. Ultrafast Frequency-Shift Dynamics at Temporal Boundary Induced by Structural-Dispersion Switching of Waveguides. *Phys. Rev. Lett.* **127**, 053902 (2021).
28. Li, H., Yin, S., Galiffi, E. & Alù, A. Temporal Parity-Time Symmetry for Extreme Energy Transformations. *Phys. Rev. Lett.* **127**, 153903 (2021).
29. Carminati, R., Chen, H., Pierrat, R. & Shapiro, B. Universal statistics of waves in a random time-varying medium. *Phys. Rev. Lett.* **127**, 94101 (2021).

## Methods

### Theoretical Design and Optimization of the Loaded Transmission Line Metamaterial

Each unit cell of our transmission line, once the switches have been activated, can be approximately modelled by the T-network shown in Fig. S1, where  $d$  is the physical length of the cell (i.e. one turn of the meandered microstrip on our printed circuit board), and  $jb = j\omega CZ_o$  is the susceptance of the capacitive load, normalized against  $Z_o$ , the characteristic impedance of the unloaded TLM. The voltage and currents at the input port of such a network can be related to those at the output port by its ABCD matrix, which reads (1),

$$\begin{bmatrix} A & B \\ C & D \end{bmatrix} = \begin{bmatrix} \left(\cos \theta - \frac{b}{2} \sin \theta\right) & j \left(\sin \theta + \frac{b}{2} \cos \theta - \frac{b}{2}\right) \\ j \left(\sin \theta + \frac{b}{2} \cos \theta + \frac{b}{2}\right) & \left(\cos \theta - \frac{b}{2} \sin \theta\right) \end{bmatrix}. \quad (\text{S1})$$

Here,  $\theta = k_o d$  is the total propagation phase through the unloaded transmission-line section. Applying Bloch boundary condition yields the dispersion relation for an infinitely long chain of this unit cell as

$$\cos(\beta d) = \cos \theta - \frac{b}{2} \sin \theta. \quad (\text{S2})$$

Furthermore, the Bloch wave impedance of the periodic structure is given by

$$Z_B = \pm \frac{BZ_o}{\sqrt{A^2 - 1}}. \quad (\text{S3})$$

In Fig. S2, we plot the normalized dispersion relation and the Bloch wave impedance of our TLM, for  $\theta = 72^\circ$  and  $b = 2.753$ . where  $\omega_o = 2\pi \times 100$  MHz is the designated maximum operating frequency. In this case, the loaded TLM to exhibit a Bloch impedance is exactly  $Z_o/2$  at  $\omega = \omega_o/2 = 2\pi \times 50$  MHz, and retains approximately the same value for lower frequencies.

Having determined the ideal frequency translation ratio  $f_2/f_1$ , as well as the wave impedances before ( $Z_1$ ) and after ( $Z_2$ ) switching, one can calculate the theoretical temporal reflection and transmission coefficient of the TLM. For generality, we present a set of parametric studies that were conducted to identify the best design parameters for the TLM, which can be scaled to accommodate different specifications (i.e., different temporal reflection magnitude and frequency translation ratios).

At the design stage, two key parameters need to be determined: the length of the unit cell, which is directly proportional to the phase accumulation; and the appropriate shunt load  $b$ . Both parameters will have significant impact on various aspects of the time interface. Crucially, together, they determine the band gaps of our TLM. Since we wish to operate in a regime in which the TLM is almost translationally homogeneous and dispersionless, we must pay special attention to avoid the first band gap. To this end, we perform parametric studies on  $R$  and  $f_2/f_1$  by sweeping  $\theta$  and  $b$  (which is equivalent to sweeping the cutoff frequency of the first band gap,  $\omega_c$ ); the results

for  $R$  and  $f_2/f_1$  are plotted in Fig. S3A and Fig. S3B respectively. In Fig. S3A, we use a red line to denote the combinations of  $(\theta, \omega_c)$  that gives the maximum temporal reflection magnitude.

### Practical Implementation

The practical circuit layout for our TLM design is shown in Fig. S4. Panel A depicts a single unit cell, while panel B depicts the connection between multiple unit cells. The circuit is fabricated using a 1.52 mm thick Rogers TMM 13i substrate, which has a dielectric constant of  $12.85 \pm 0.35$ , and a loss tangent of 0.0019. Table S1 lists all the circuit components used in our design.

### Circuit Simulations

All circuit simulations are performed in Keysight Advanced Design Systems (2). Time domain simulations are carried out using the Transient solver, while frequency domain analysis is done with the S-Parameters solver.

The main TLM carrying the signal is modelled with physical transmission line sections with characteristic impedance  $Z_o = 50 \Omega$ , length  $d = 0.208$  m, effective dielectric constant  $\epsilon_{r,eff} = 8.36$ , attenuation constant  $\alpha = 0.5$  (at  $f = 100$  MHz, dielectric loss tangent  $\tan \delta = 0.0019$ ). It should be noted that the effective dielectric constant of 8.36 is consistent with expectations from well-known design formulas with microstrip lines<sup>1</sup>. To further model the non-idealities associated with our manufactured circuit, each unit cell is connected to its nearest with a 2 pF capacitor, and to its second nearest neighbor with a 1 pF capacitor. This models the parasitic capacitive coupling between the unit cells, which limits our operating bandwidth by introducing dispersion and bandgaps. These values are found to produce consistently good match between experimental and simulation results.

The switches are implemented as ideal voltage controlled reflective switches with  $1 \Omega$  resistance in the “on” state. Each switch connects a node on the transmission line to a series RLC circuit, with an 82 pF capacitor representing the load, a  $4 \Omega$  resistor representing the parasitic losses, and an 8 nH inductor representing the parasitic inductance of the grounding vias. These values are extracted from measurements with a single unit cell.

### Time Domain Observation of Temporal Reflections

A simplified schematic of our experimental set up for time domain measurements is shown in Fig. S5. The input signal is launched from an arbitrary waveform generator (Keysight M8195A) into a symmetric power splitter. Identical copies of the input (both with 3.5 dB attenuation) are fed to Port 1 of the transmission line as well as channel 1 of an oscilloscope (Tektronix DPO4104), which records  $V_1(t)$ . Port 2 of the transmission line is connected to channel 2 of the oscilloscope, which records  $V_2(t)$ . Both oscilloscope channels have an input impedance of  $50 \Omega$ , and are record in the averaged mode with 512 samples.

During our measurements, the input signal consists of a 5kHz pulse train formed by repeated copies of an arbitrarily shaped pulse. Since our input pulses generally have durations in the order of tens of ns, which is much shorter than the period of the pulse train, we can effectively treat each pulse as a single isolated event. To control the switches, we use a rectangular pulse train that is

phased locked to the input pulse train. By adjusting the relative phase between the two signals, we can control when the input pulse experiences the time interface. Notably, the switch that we used has internal grounding circuitry which ensures the load capacitors begin each cycle of measurement completely discharged<sup>3</sup>. This is crucial for the accurate implementation of the temporal boundary condition, which demands charge discontinuity.

To observe the temporal reflection, we activate the switches after the input signal is registered in  $V_1(t)$ , but before it is recorded in  $V_2(t)$ , corresponding to a time when the signal is completely contained within the TLM. The time-reflected signal will travel backwards towards Port 1 of the transmission line, where it will again enter the input power splitter. Identical copies of the time-reflection (with 3.5 dB attenuation) are fed to the source and the oscilloscope. Hence, the actual amplitude of the temporal reflection generated by our time interface is larger than that recorded in  $V_1(t)$ .

### Exact Timing of the Temporal Interface

Ideally, we should be able to calculate the exact moment when the time interface was activated, based on the instance at which the switch control signal passed the logic threshold, and the manufacturer-supplied datasheet<sup>3</sup>. In reality, this is made difficult by a variety of non-idealities, such as finite signal rise times in the circuit, and the component tolerances for the switches. Hence, we use the following procedure to experimentally deduce the precise moment when the time interface is formed.

We begin by placing the rising edge of the control signal at some arbitrary time during the first pass of the input signal through the transmission line. This will generate a time reflection which returns to the input after a certain time delay  $\delta$ . We then slowly adjust the phase between the control signal and the input signal, which affects the time passage between the injection of the signal and the activation of the time interface. This will in turn change the delay  $\delta$ , which can be directly measured in  $V_1(t)$ . We continue tuning the phase, while trying to reduce  $\delta$ , until the time-reflected signal is observed immediately after the input signal. This indicates that the time interface was activated precisely after the complete injection of the signal.

### Measurement of Broadband Frequency Translation Ratio

To measure the frequency translation ratio of our time-interface, we launched signals with varying carrier frequencies into the transmission-line, and observed the time-reflected as well as transmitted signals. A typical time domain measurement is shown in Fig. S6. We performed Fourier analysis on the time-gated incident, transmitted, and reflected signals to observe their individual frequency content. The frequency spectra for each signal will consist of a sharp peak, aligned with its center frequency. We define the frequency translation ratio for the reflected ( $\xi_r$ ) and transmitted ( $\xi_t$ ) waves as  $\xi_{r,t} = f_{2,peak}^{(r,t)} / f_{1,peak}$ , where  $f_{2,peak}^{(r,t)}$  are the peak frequencies of the reflected and transmitted signals, and  $f_{1,peak}$  is that of the incident signal.

### Retrieval of the Time-Reflection and Time-Transmission Coefficients

In our experimental setup, we measured the signal at the input port at  $x = 0$  as  $V_1(t)$  in the main text, which is a linear superposition of input and time-reflected signals. Considering the effect

of the power splitter that connects the source (denoted by subscript “s”), transmission-line (subscript “t”), and the oscilloscope (subscript “o”), we can write

$$V_1(t) = \mathcal{F}^{-1} \left\{ S_{os}(\omega) \frac{\mathcal{F}[V_{inc}(0, t)]}{S_{ts}(\omega)} + S_{ot}(\omega) \mathcal{F}[V_{ref}(0, t)] \right\}, \quad (\text{S4})$$

where  $\mathcal{F}$  denotes the Fourier transform.  $S$ -parameters measurement of the splitter gives  $S_{os} \approx S_{ts} \approx S_{ot} \approx 0.665$  from 10~100 MHz.

The reflection coefficient at a time-interface at  $t = t_s$  is defined as

$$R(k) = \frac{\tilde{V}_{ref}(k, t_s^+)}{\tilde{V}_{inc}(k, t_s^-)} = \frac{\int_{-\infty}^{+\infty} V_{ref}(x, t_s^+) e^{jkx} dx}{\int_{-\infty}^{+\infty} V_{inc}(x, t_s^-) e^{jkx} dx}, \quad (\text{S5})$$

where  $k$  is the real part of the wavenumber conserved across the time-interface.  $\tilde{V}_{inc,ref}(k, t)$  refer to the incident and reflected signals in the momentum space, while  $V_{inc,ref}(x, t)$  are the voltages expressed in the real space. We assume that the dispersion and the loss of the transmission line are small enough:  $\omega \approx vk$  and then  $V_{inc}(x, t) \approx V_{inc}(0, t - \frac{x}{v_1}) e^{-\alpha_1 x}$ ,  $V_{ref}(x, t) \approx V_{ref}(0, t + \frac{x}{v_2}) e^{\alpha_2 x}$ . The loss rates  $\alpha_1$  and  $\alpha_2$  can be retrieved by measuring the  $S$ -parameters of the unloaded and loaded transmission lines, respectively. By taking Fourier transform of the incident and reflected signals recorded at the input port, one can calculate the reflection coefficient measured at the input port for a given wavenumber  $k$  and corresponding frequencies  $\omega_{1,2}$ :

$$\begin{aligned} \tilde{R}(k) &= \frac{\mathcal{F}[V_{ref}(0, t)]|_{\omega_2}}{\mathcal{F}[V_{inc}(0, t)]|_{\omega_1}} \approx \frac{e^{-jkx} \int_{-\infty}^{+\infty} V_{ref}(0, t + \frac{x}{v_2}) e^{-j\omega_2 t} dt}{e^{jkx} \int_{-\infty}^{+\infty} V_{inc}(0, t - \frac{x}{v_1}) e^{-j\omega_1 t} dt} \\ &\approx e^{-j2kx} e^{-(\alpha_1 + \alpha_2)x} \frac{\int_{-\infty}^{+\infty} V_{ref}(x, t) e^{-j\omega_2 t} dt}{\int_{-\infty}^{+\infty} V_{inc}(x, t) e^{-j\omega_1 t} dt}. \end{aligned} \quad (\text{S6})$$

To obtain the exact temporal reflection coefficient, we need to compensate both the phase and loss during the round trip that a wave travels. Without loss of generality, we assume  $t_s = 0$ . Then, by changing the integration variable  $t = -x_r/v_1$  for the denominator and  $t = -x_r/v_2$  for the numerator in Eq. (S6), we obtain the relation between the corrected reflection coefficient and that measured at the input port:

$$R(k) \approx \frac{\omega_2}{\omega_1} \tilde{R}(k) e^{j2kx_r} e^{(\alpha_1 + \alpha_2)x_r}, \quad (\text{S7})$$

Here,  $x_r$  entails the physical distance that a wave travels from the input port until it gets reflected by the time-interface, which can be retrieved via  $x_r \approx -\frac{1}{2} \partial_k [\arg(\tilde{R})]$ .

Therefore, the procedure for retrieving the time-reflection coefficients for a given wavenumber  $k$  can be summarized as follows:

- a) Measure the  $S$ -parameters and the dispersion diagrams of unloaded and loaded transmission lines.
- b) Read the corresponding frequencies  $\omega_{1,2}$ ; Retrieve the loss rate  $\alpha_{1,2}$  from the  $S$ -parameters.
- c) Calculate the reflection coefficient at the input port  $\tilde{R}(k)$  using Eq. (S6).
- d) Compensate the loss and accumulated phase using Eq. (S7).

Similar procedure also applies to retrieving the transmission coefficient, where the relation between the transmission coefficient  $\tilde{T}(k)$  referred to two ports and the actual temporal transmission coefficient  $T(k)$  reads:

$$T(k) \approx \frac{\omega_2}{\omega_1} \tilde{T}(k, x) e^{jkL} e^{(\alpha_1 x_r + \alpha_2 x_t)}, \quad (\text{S8})$$

where  $L = x_r + x_t$  is approximately the total length of our transmission-line, and  $x_t$  denotes the retrieved distance that the wave travels after the time-interface until it exits the transmission-line.

### Derivation of the Temporal Scattering Coefficients

Consider a homogeneous transmission-line (TL) whose distributed capacitance can be changed instantaneously at  $t = 0$ , by closing or opening a switch connected to a shunt capacitor  $C_p$ , as shown in Fig. S7. The values of the capacitance are chosen such that the effective distributed capacitance of the TL stays at  $C_1$  for  $t < 0$  while it jumps to  $C_2$  for  $t > 0$ . Applying a Laplace transform  $\mathcal{L}\{v(t)\} = \int_0^{+\infty} v(t) e^{-st} dt = V(s)$  on both voltage  $v(z, t)$  and current  $i(v, t)$ , one can write the wave equation for  $t > 0$  as:

$$(\partial_z^2 - s^2 L_1 C_2) V = -L_1 C_1 (s + j\omega_1) v(z, 0^-). \quad (\text{S9})$$

Assuming a harmonic variation  $e^{-jkz}$  of the fields in space, we can solve for the voltage in  $s$ -domain. For connecting a parallel capacitor as shown in Fig. S7A,

$$V(z, s) = \frac{C_1 s + j\omega_1}{C_2 s^2 + \omega_2^2} v(z, 0^-), \quad (\text{S10})$$

while for the case of opening the switch as shown in Fig. S7B,

$$V(z, s) = \frac{s + j\frac{C_1}{C_2}\omega_1}{s^2 + \omega_2^2} v(z, 0^-). \quad (\text{S11})$$

In both cases,  $\omega_2$  is not only the eigenfrequency of the TL after switching, but also relates to the poles of the fields in  $s$ -domain. It reads:

$$\omega_2 = \omega_1 \sqrt{C_1/C_2} = \omega_1 Z_2/Z_1, \quad (\text{S12})$$

which predicts the theoretical frequency translation ratio.

More interestingly, by applying the initial-value theorem, Eqs. (S10) and (S11) will entail different temporal boundary conditions: when closing the switch (Fig. S7A) the voltage is discontinuous and the charge stored in capacitors is conserved:

$$C_2 v(z, 0^+) = C_1 v(z, 0^-), \quad (\text{S13})$$

while in the case where the switch is opened (Fig. S7B), the voltage remains continuous, yet the charges are not because  $C_p$  is suddenly disconnected from the TL system:

$$v(z, 0^+) = v(z, 0^-). \quad (\text{S14})$$

Numerical examples of these two cases are demonstrated in Fig. S7C and D: when connecting  $C_p$  such that  $C_2 = 4C_1$ , the voltage on the TL is discontinuous at  $t = 0$ , while the total charge in the system is conserved, though part of the charge stored in  $C_1$  is transferred to  $C_p$  instantaneously. The frequency is halved as expected. By contrast, when disconnecting  $C_p$  from the TL such that  $C_2 = C_1/4$ . The voltage is continuous across the time-interface, while the total charge decreases as we exclude  $C_p$  from the system. The frequency doubles as expected in this case.

Having derived these boundary conditions, we can readily find the temporal reflection and transmission coefficients for switching on a parallel capacitor:

$$\begin{aligned} T_{on} &= \frac{1}{2} \left( \frac{C_1}{C_2} + \sqrt{\frac{C_1}{C_2}} \right) = \frac{Z_{on}(Z_{on} + Z_{off})}{2Z_{off}^2}, \\ R_{on} &= \frac{1}{2} \left( \frac{C_1}{C_2} - \sqrt{\frac{C_1}{C_2}} \right) = \frac{Z_{on}(Z_{on} - Z_{off})}{2Z_{off}^2}; \end{aligned} \quad (\text{S15})$$

and for switching off a parallel capacitor:

$$\begin{aligned} T_{off} &= \frac{1}{2} \left( 1 + \sqrt{\frac{C_1}{C_2}} \right) = \frac{Z_{on} + Z_{off}}{2Z_{on}}, \\ R_{off} &= \frac{1}{2} \left( 1 - \sqrt{\frac{C_1}{C_2}} \right) = \frac{Z_{on} - Z_{off}}{2Z_{on}}. \end{aligned} \quad (\text{S16})$$

In our experiments with temporal slabs, we observed two time-reflected signals, and both are out of phase with respect to the incident signal. This can only be explained via Eqs. (S15) and (S16): in fact, in our setup the effective impedance is decreased when the loaded capacitors are switched on, i.e.,  $Z_{on} < Z_{off}$ , and vice versa. Both temporal reflection coefficients  $R_{on,off}$  will be negative,

hence, both time-reflected waves ( $R_{on}T_{off}$  and  $T_{on}R_{off}$ ) will be out of phase to the incidence, while the two time-transmitted waves ( $T_{on}T_{off}$  and  $R_{on}R_{off}$ ) will be in phase.

## Extended Data

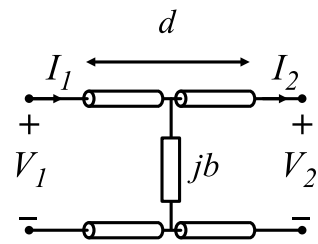


**Fig. S1.**

Equivalent T-network for one unit cell of our TLM when the switches are closed. Here,  $d$  is the physical length of the unit cell (0.2080m) and  $jb = j2.753$  is the normalized load susceptance at 100 MHz.

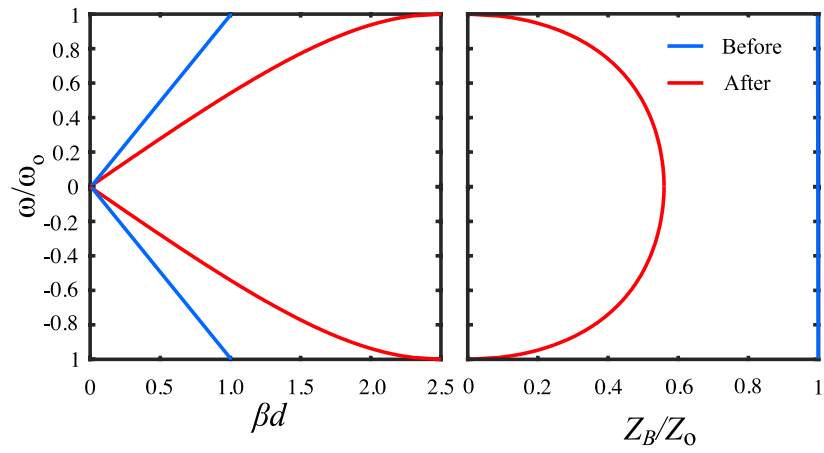


**Fig. S2.**

Normalized dispersion relation and Bloch impedance of our transmission line, assuming an unit-cell electrical length of  $\theta = kd = 72^\circ$ , and an normalized load susceptance of  $b = 2.753$ , both evaluated at 100 MHz. The blue lines and the red lines correspond to the unloaded and the loaded lines respectively.

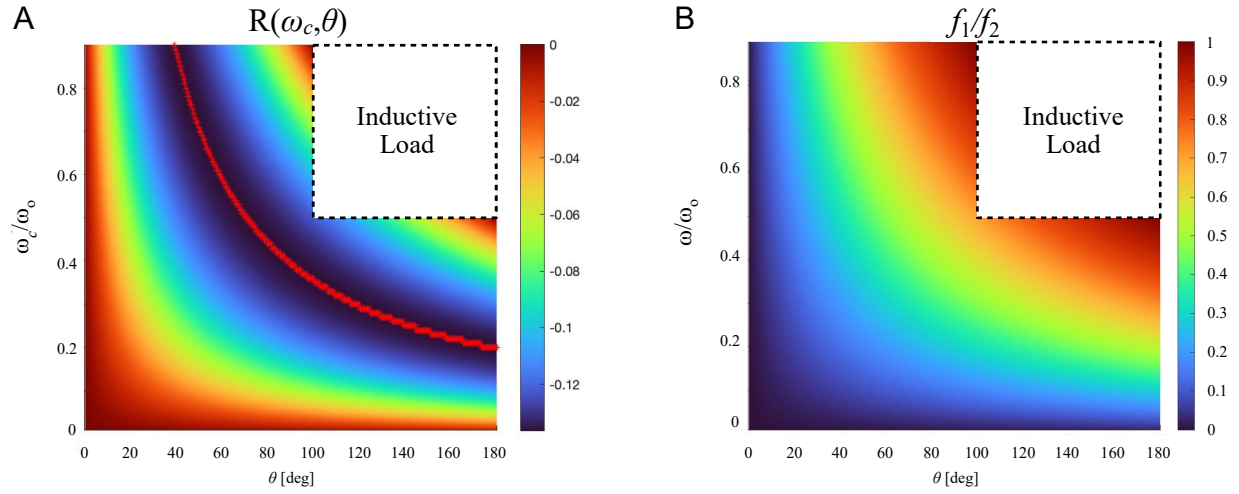


**Fig. S3.**

Parametric study for the identification of the optimal unit-cell electrical length  $\theta$  and cutoff frequency of the first band gap  $\omega_c$ , which is related to the load susceptance  $b$ . **(A)** A map for the temporal reflection coefficient and **(B)** a map for the frequency translation ratio. The red line in panel A corresponds to the combination of  $(\theta, \omega_c)$  that yields the largest reflection coefficient. The white boxes with dotted border in both panels denote regions in which the load susceptance become inductive (i.e., negative).

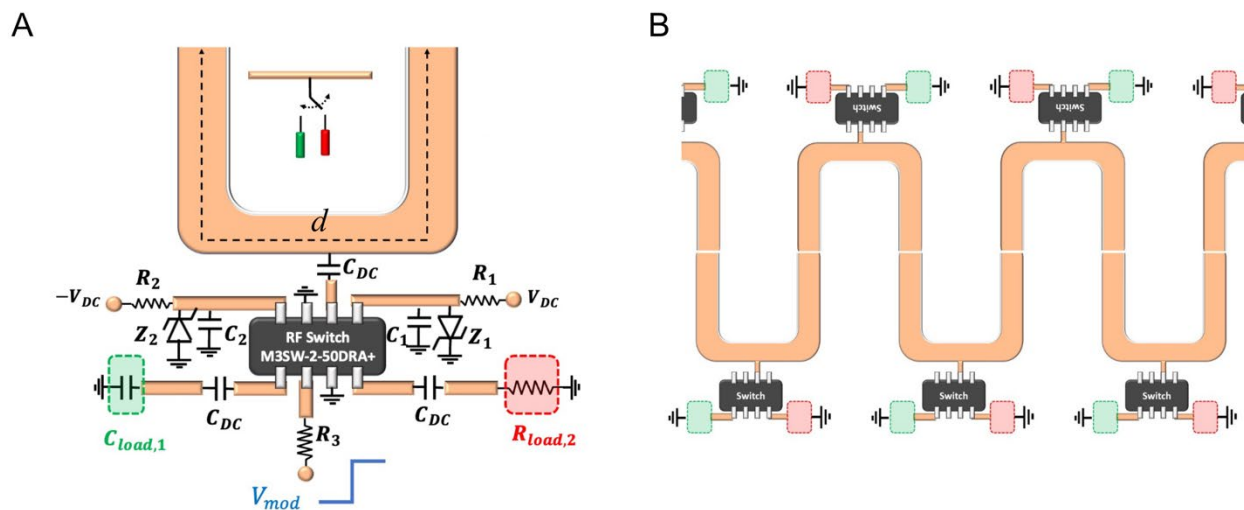


**Fig. S4.**

Circuit layout for the fabricated transmission line. **(A)** Layout for the unit cell. The descriptions of the components can be found in Table S1. **(B)** Schematic for the complete TLM, showing how the unit cells are connected.

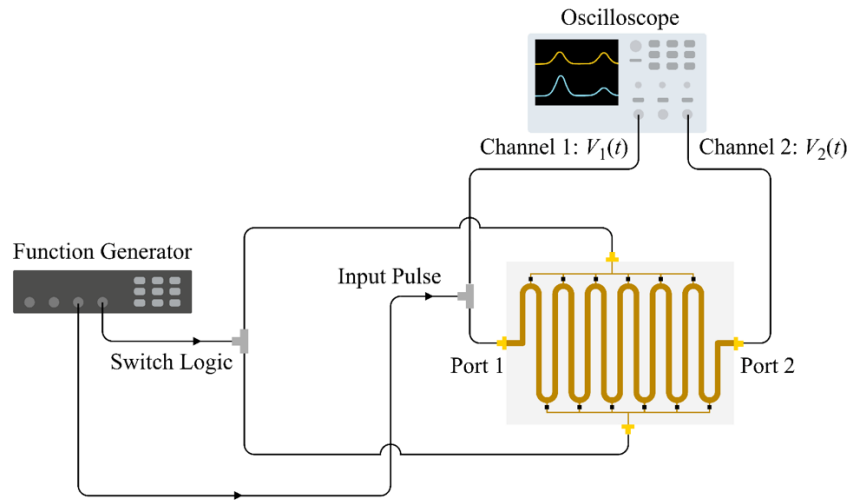


**Fig. S5.**

Simplified schematic of the experimental set up for time domain measurements. Power supply for the switches and a separate function generator for switch control are not shown.

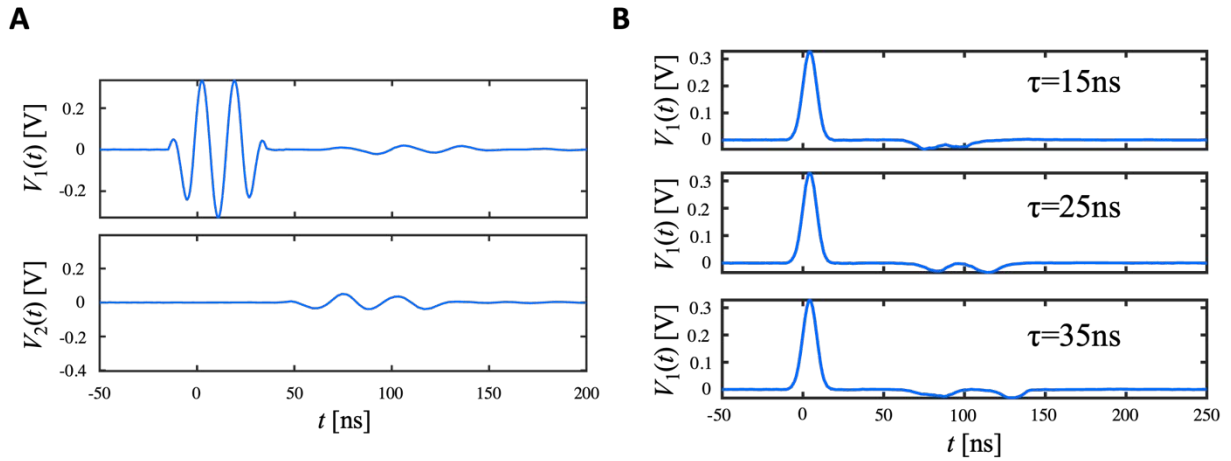


**Fig. S6.**

Samples of time-domain measurements. **(A)** A measurement used to determine the frequency translation ratio. The top plot depicts the incident and the TR signals, while the bottom plot depicts the transmitted signal. The effect of frequency translation is immediately obvious from the increased period of the TR and transmitted signals. A Fourier analysis on the time-gated incident, reflected and transmitted signals, followed by a comparison of their spectral peaks, gives Fig. 2F in the main text. **(B)** Measured waveform at the input port for various values of slab duration  $\tau$ . As  $\tau$  increases, so does the delay between the two TR signals. Fourier analysis on the time-gated reflected signals is used to construct Fig. 3D and Fig. 3E in the main text.

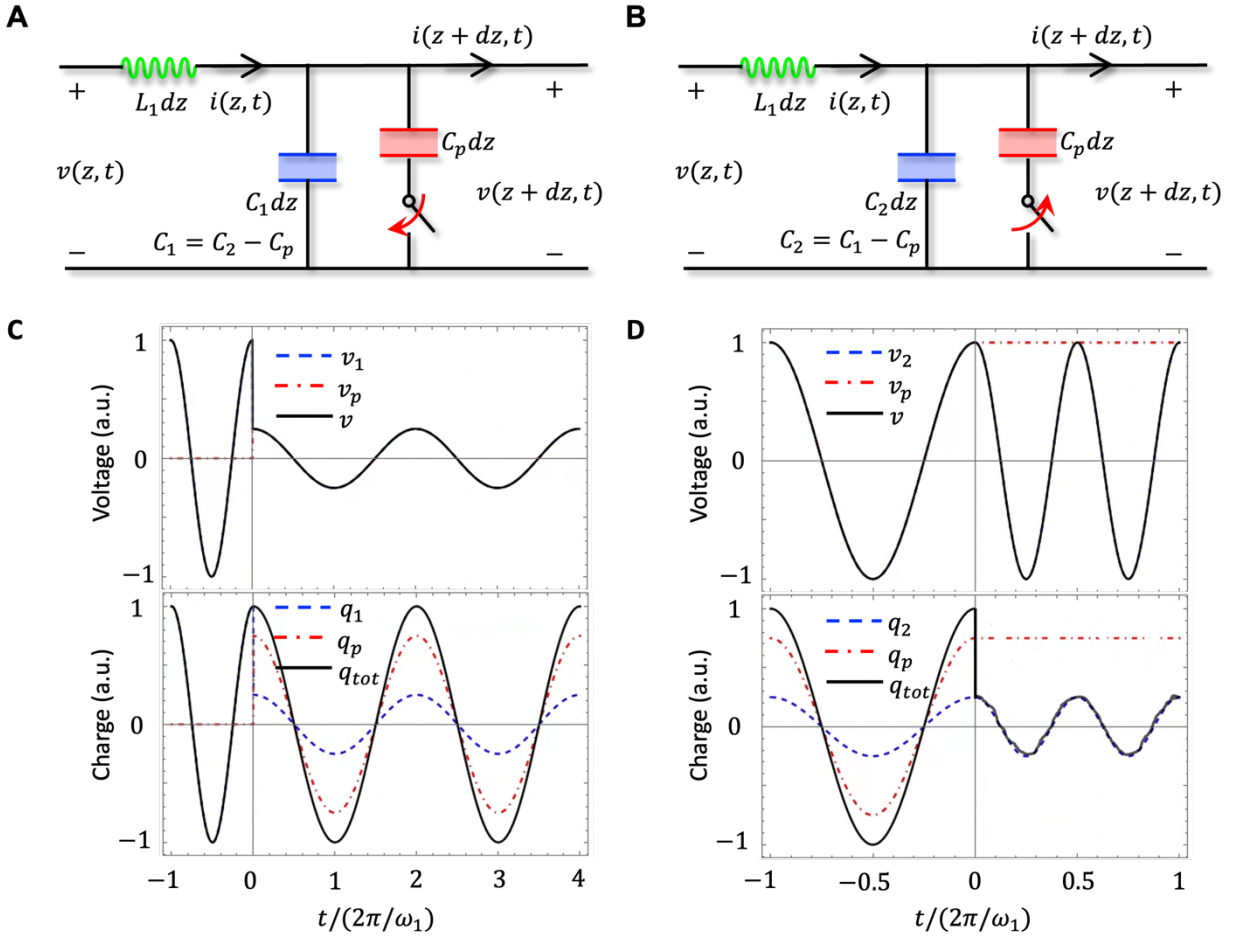


**Fig. S7.**

Circuit model of time-switched transmission-line (TL), with the (A) loading, and (B) removal of a parallel capacitor.  $C_1(C_2)$  denotes the value of effective distributed capacitance of the TL before (after) closing or opening the switch. Panel C demonstrates the time variation of voltages and charges on each capacitor, as well as their total values sensed by the TL, corresponding to a numerical example of Panel A with  $C_2 = 4C_1$ . Panel D shows the same quantities for a numerical example of Panel B with  $C_2 = C_1/4$ .

**Table S1.**

List of components used to fabricate our transmission line, referred to the schematic shown in Fig. S4.

Component	Description	Value	Component Number
$C_{DC}$	DC blocking capacitor	3.900 nF	C0402C392K5RACAUTO
$C_{1,2}$	RF shorting capacitor	10 pF	06031A100GAT2A
$R_{1,2}$	Resistor	11.5 Ohm	RK73H1JTDD11R5F
$R_3$	Resistor	100 Ohm	RK73H1JTDD1000F
$Z_{1,2}$	Zener Diode	$V_z = 5.3 V$	MMSZ4690T1G
RF Switch			M3SW-2-50DRA+
$R_{load,2}$	TL load (OFF-State)	1 MOhm	RCS12061M00JNEA
$C_{load,1}$	TL load (ON-State)	82 pF	C0402C823K9RACTU

## References

1. D. M. Pozar, *Microwave Engineering* (John Wiley & Sons, 2011).
2. Keysight, PathWave Advanced Design System. *Keysight*, (available at <https://www.keysight.com/us/en/products/software/pathwave-design-software/pathwave-advanced-design-system.html>).
3. Minicircuits Fast Switching SPDT RF Switch, (available at <https://www.minicircuits.com/pdfs/M3SW-2-50DRA+.pdf>).